

X-ray Emission from the Warm-Hot Intergalactic Medium

E. Ursino and M. Galeazzi¹

Physics Department, University of Miami, Coral Gables, FL 33155

Received _____; accepted _____

arXiv:astro-ph/0604175 v2 10 Apr 2006

¹corresponding author, galeazzi@physics.miami.edu

ABSTRACT

The number of detected baryons in the Universe at $z < 0.5$ is much smaller than predicted by standard big bang nucleosynthesis and by the detailed observation of the Lyman alpha forest at red-shift $z = 2$. Hydrodynamical simulations indicate that a large fraction of the baryons today is expected to be in a “warm-hot” (10^5 - 10^7 K) filamentary gas, distributed in the intergalactic medium. This gas, if it exists, should be observable only in the soft X-ray and UV bands. Using the predictions of a particular hydrodynamic model, we simulated the expected X-ray flux as a function of energy in the 0.1-2 keV band due to the Warm-Hot Intergalactic Medium (WHIM), and compared it with the flux from local and high red-shift diffuse components. Our results show that as much as 20% of the total diffuse X-ray background (DXB) in the energy range 0.37-0.925 keV could be due to X-ray flux from the WHIM, 70% of which comes from filaments at redshift z between 0.1 and 0.6. Simulations done using a FOV of $3'$, comparable with that of Suzaku and Constellation-X, show that in more than 20% of the observations we expect the WHIM flux to contribute to more than 20% of the DXB. These simulations also show that in about 10% of all the observations a single bright filament in the FOV accounts, alone, for more than 20% of the DXB flux. Red-shifted oxygen lines should be clearly visible in these observations.

Subject headings: diffuse radiation, large-scale structure of universe (WHIM), X-rays: diffuse background

1. Introduction

The detailed observation of the Lyman alpha forest at red-shift $z = 2$, the result from the WMAP experiment, and the observation of the light element ratio combined with standard nucleosynthesis, all point to the baryon density (expressed as a present day fraction of the closure density of the universe) Ω_B , being about 0.04 (Rauch et al. 1998; Weinberg et al. 1997; Burles & Tytler 1998; Kirkman et al. 2003; Bennett et al. 2003). In contrast, integrating the observed mass distribution function of stars, galaxies and clusters, the baryonic fraction of the local universe (Fukugita et al. 1998)($z \sim 0$) appears to be about a factor of 2 to 4 times lower.

Where is the missing baryonic mass at $z \sim 0$? The state of these missing baryons can be computed from standard initial conditions in realistic large-scale cosmological hydrodynamic simulations (Cen & Ostriker 1999; Croft et al. 2001; Borgani 2004; Yoshikawa et al. 2003). Both theoretical and recent observational work (Tripp & Sandage 2002) suggest that much of the “missing” material lies in a “warm-hot” filamentary gas, distributed in the intergalactic medium (WHIM), with temperature between 10^5 and 10^7 K, which makes it very difficult to observe. The best theoretical estimates of its distribution in space and temperature indicate that the bulk of the material lies in regions with a density between 20-1000 times the average density of the universe, and has a temperature greater than 5×10^5 K, which essentially makes it invisible to all but low energy X-ray observations.

There have been several recent measurements that offer tantalizing hints on the existence of this material. Both Chandra (Nicastro et al. 2002; Fang et al. 2002) and XMM (Rasmussen 2002; Rasmussen 2003) grating observations have detected resonance O VII and O VIII absorption lines along the lines of sight to several distant quasars and BL Lac objects. Most of the observed features lie near zero velocity, suggesting that they may be caused by hot gas in our own Galaxy or in the Local Group. Simple estimates of the mass

and temperature of this material indicate that it may dominate the baryon content of the Local Group and has a temperature near 2×10^6 K, consistent with the virial temperature of the Local Group. Assuming that the Local Group is representative of other spiral-rich groups, which contain the bulk of all galaxies in the universe, these observations alone would more than double the census of observable baryons. As shown by Mulchaey et al. (2003), the existence of such low temperature flux would explain much of the ROSAT data for spiral-rich groups. ROSAT imaging and spectroscopy (Zappacosta 2002; Scharf 2000) suggest the existence of several X-ray “filaments” or clumps that are not obviously associated with rich clusters or groups. Their properties are similar to those predicted in numerical simulations of the Intergalactic Medium (IGM), but the low quality of the data prevents strong conclusions. A recent observation (Nicastro et al. 2005) found absorption lines at redshift significantly greater than 0 ($z=0.011$, $z=0.027$). This seems to indicate the presence of absorbers out of the Local Group. These data can be used to estimate the abundance of filaments on a line of sight as $dP/dz = 67_{-43}^{+88}$, however only one observation is available at this point and the sensitivity of current experiments does not permit to improve the statistics past this one data point.

In addition to the resonant absorption line in the lines of sight of distant quasars and BL Lac objects just mentioned, three different approaches have been proposed for detecting the WHIM. All methods rely on the detection of the X-ray flux from the WHIM on top of the foreground due to the flux from the Local Bubble and the Galactic halo and the background due to very distant point sources.

1. Red shifted ($z < 1$) strong soft X-ray emission lines from highly ionized elements (such as O VIII 653 eV line) should be observable (Galeazzi et al. 2000; Galeazzi et al. 2004).
2. The filamentary structure of the WHIM should generate a characteristic angular pattern in the soft X-ray flux that can be detected using the angular autocorrelation

function (Soltan et al. 1996; Soltan et al. 2001; Croft et al. 2001).

3. Search for shadows of the more distant WHIM cast by nearby galaxies that are rich in neutral hydrogen (Barber et al. 1996; Bregman & Irwin 2001).

The first of the three methods is the one that promises the best results since, in addition to the detection of the WHIM, it could provide also a tool to study the characteristics of the gas. In this work we used the prediction of the hydrodynamic model of Cen and Ostriker (1999, Cen99 from here on) to simulate the expected X-ray flux due to the WHIM, to determine its detectability and expected characteristics. This will offer a tool to determine the effect of the WHIM on future and present missions and to possibly design a future mission dedicated to the study of the WHIM. Our investigation has been focused on the soft X-ray spectrum between 50 eV and 2000 eV, with special attention to the O VII and O VIII lines. The results are in the form of energy spectra and images. It has been possible to derive general characteristics of the WHIM, and how the WHIM may be detected and may affect future experiments.

2. The Model

The starting point of our simulations are the results of the hydrodynamic simulation of Cen and Ostriker (Cen99). Among other results, this simulation gives a set of three cubes $100 \text{ Mpc } h^{-1}$ in size [$h = H_0/(100 \text{ km s}^{-1} \text{ Mpc}^{-1})$, with H_0 being the current time Hubble constant], with $512 \times 512 \times 512$ elements, containing temperature, metallicity (as fraction of the solar one), and overdensity (ρ/ρ_0 , with ρ_0 being the critical density of the Universe) for the intergalactic medium at $z=0$ (Cen's cubes from here on). We used Cen's cubes to build a 3D representation of the intergalactic medium up to $z=2$ piling up several cubes. As will be discussed in more details later on, we didn't go to higher redshift because

there is no significant soft X-ray flux beyond $z=2$. To limit the effect of periodicity (i.e., finding the same structure in the same position every time), each cube is randomly rotated, shifted, and the coordinates are permuted, so that each cube could have 24,576 different configurations. The values of temperature, metallicity and overdensity of each element are also rescaled depending on the red-shift of the element, following the expected average changes reported by Cen and Ostriker (1999, 2001).

To determine the X-ray flux due to the WHIM, an arbitrary starting point is chosen in the first cube and a conical field of view (FOV) is generated with an angular aperture that can be arbitrarily chosen at the beginning of the simulation. Among all the elements that fit in the field of view, only those belonging to the WHIM are selected. For the selection we followed the indication of Cen and Ostriker (Cen99), and excluded elements with temperature above 10^7 K and/or overdensity above 1000 (clusters of galaxies), and elements with temperature below 10^5 K (cool gas). This selection works quite well at identifying clusters of galaxies and other regions that don't contribute to the X-ray flux from the intergalactic medium. However, in our analysis we observed a residual flux of X-rays coming from the outer regions of galaxy clusters. Our results may therefore somewhat overestimate the true intergalactic flux. For each element with values of temperature and density within our acceptable parameters, an X-ray spectrum is generated. The spectra are then added together to generate the X-ray spectrum due to the WHIM. The spectra are generated using the APEC thermal model included in the code XSPEC¹. Even for a FOV of a few arcmin, several million elements are included in the FOV, making the call to XSPEC for each element unfeasible. We therefore generated a matrix of 1470 spectra, using forty-nine different values of temperature equally spaced on a logarithmic scale from 2.5×10^5 K to 1.18×10^8 K, and thirty values of metallicity, equally spaced on a logarithmic

¹<http://heasarc.gsfc.nasa.gov/docs/xanadu/xspec/>

scale from 5×10^{-5} to 5 (expressed as fraction of the solar metallicity), with the higher limit due to the APEC model limitations. The spectra were generated using solar abundances, according to the model by Anders and Grevesse (1989). Each spectrum is then obtained as the weighted average of the four spectra in our matrix with values of temperature and metallicity closer to the element values. For elements at the edge of the FOV, the spectral amplitude is also scaled based on the fraction of the element that fits in the FOV. This is particularly important for small FOV's, and for elements at low redshift. Failing to perform this rescaling, would result in a significant overestimate of the WHIM X-ray flux. Galactic absorption is applied at the end of the simulation using the model by Morrison and McCammon (1983). For the current analysis, we adopted a typical high latitude column density value of $1.80 \times 10^{20} \text{ cm}^{-2}$ (McCammon et al. 2002).

3. Results

For the analysis we adopted three different FOV's, equal to 3', 10', and 30'. A FOV of 3' is comparable to what is expected for Constellation-X ², while 30' is comparable to that of XMM-Newton ³. The FOV of 10' has been chosen as an intermediate value.

Most of the results reported here focus on the energy interval 0.375 – 0.950 keV. The upper limit of this energy range has been chosen to include the emission from Ne IX and the strong Fe XVII lines from 0.725 to 0.827 keV. The lower limit has been chosen as to consistently exclude the strong C VI lines at 0.367 keV. This makes us sensitive to O VII out to redshifts of $z=0.5$. A lower limit well above 0.284 keV is also advantageous to avoid instrument effects due to the neutral carbon absorption edge which is present in most

²<http://constellation.gsfc.nasa.gov/mission/overview/index.html>

³http://xmm.vilspa.esa.es/external/xmm_user_support/documentation/uhb/node14.html

instruments. Our simulations indicate that, in this energy band, the average flux due to the WHIM is 6.9 ± 0.9 photons $\text{cm}^{-2} \text{s}^{-1} \text{sr}^{-1}$. Compared with the expected total flux in the same energy range due to the DXB of 29.3 photons $\text{cm}^{-2} \text{s}^{-1} \text{sr}^{-1}$ (derived using data from McCammon et al. 2002, Table 3), our result indicates that as much as 20% of the diffuse X-ray background could be due to X-ray flux from the WHIM. This is an upper limit to the X-ray flux from the WHIM as, with our data selection, it may still include flux from the outer regions of galaxy clusters.

We also studied the evolution of the WHIM flux with increasing redshift. We split the column along the line of sight in 30 intervals, each interval corresponding to one Cen’s cube (this is not a linear spacing in redshift) and we saved the data of the flux calculated for each interval. Figure 1 shows the distribution of the WHIM flux as a function of redshift. We found that, in the energy range we used for our analysis, the X-ray flux due to the WHIM is approximately constant with redshift up to $z \sim 0.5$ and that 70% of the total flux comes from gas at redshift between 0.1 and 0.6. At redshifts higher than 0.6 the X-ray flux drops quickly both because emission lines are shifted outside the energy range and because the density of the gas becomes significantly smaller. In particular, the two steps in the X-ray flux at $z \sim 0.5$ and $z \sim 0.7$ are due to the fact that at those values the O VII and O VIII lines respectively are redshifted outside the energy range. The figure also shows that, in the energy range considered, there is no significant X-ray emission from gas at redshift higher than 1.

Of particular interest for the design of a mission to design the properties of the WHIM is how the X-ray flux changes for different FOV’s. While the average of the flux over several simulation obviously does not depend on the FOV, the distribution of the flux from individual simulations strongly depends on it. In Figure 2 we reported the flux distribution of the simulations for the three FOV’s. This gives the probability that an observation

would detect a specific flux due to the WHIM. In the case of 3' FOV most observations don't encounter any bright X-ray emitting region (a “filament” of the WHIM) and the X-ray flux is close to zero. When a bright filament is encountered, however, the flux can reach very high values. The distribution of the flux per run looks almost exponential, with a maximum for very small flux (around 1 photon $\text{cm}^{-2} \text{s}^{-1} \text{sr}^{-1}$), and with a reasonable number of simulations that show a very high X-ray flux. In the case of 30' FOV, instead, several filaments tend to always be in the FOV and the distribution is much narrower and peaked around the average value of 6.9 ± 0.9 photons $\text{cm}^{-2} \text{s}^{-1} \text{sr}^{-1}$. The distribution of the 10' FOV runs is in between these two cases. Of relevance for current and future missions is actually the integral of the distribution reported in Fig. 2. This, in fact, for each value reported on the x-axis, gives the probability that an observation will detect an X-ray flux due to the WHIM greater than that value. The result is shown in Fig. 3. From the figure we can see, for example that with a 3' FOV, in about 20% of the observations we expect the WHIM flux to contribute to more than 20% of the DXB (5.8 photons $\text{cm}^{-2} \text{s}^{-1} \text{sr}^{-1}$).

This value alone is not sufficient to determine if a mission would be able to observe and study the X-ray flux from the WHIM. In fact, even when the X-ray flux is relatively high, if it's due to gas distributed at different redshifts it will show up in an observation almost as a continuum distribution, which is very difficult to separate from the other DXB flux. If, on the other end, the majority of the flux comes from gas at the same redshift (i.e., a single filament), then emission lines at that specific redshift are observable. We therefore split our FOV in small slices of redshift, approximately 0.03 thick (equivalent to the size of one Cen's cube), and we looked at the number of times that in each simulation the flux coming from a single slice was above a threshold equal to either 10% or 20% of the total DXB flux (i.e., 2.9 and 5.8 photons $\text{cm}^{-2} \text{s}^{-1} \text{sr}^{-1}$). Figure 4 shows the result of this analysis for the 3' FOV simulations. The result indicates that in almost 10% of all the observations a single bright filament in the FOV accounts, alone, for more than 20% of

the DXB flux. This means that in almost 10% of the cases we expect to have most of the WHIM flux concentrated at a single red-shift. We therefore expect to observe O VII and O VIII lines at that red-shift with an estimated flux of more than 5 photons cm⁻² s⁻¹ sr⁻¹. The same analysis repeated for 10' FOV and 30' FOV shows that, while the probability of having a high X-ray flux increases as the FOV is increased, the probability of having a significant amount of flux coming from a single redshift decreases drastically. To be able to detect and study the properties of the WHIM using X-ray flux an angular resolution of a few arcminutes is therefore necessary.

4. Angular extension of the WHIM filaments

The analysis of spectra from objects in a narrow field of view gives us useful information about the flux properties of the WHIM, and hints about its distribution, and detectability. However, to better understand the angular properties of the WHIM we also generated images in the soft X-ray band.

We chose a field of view of 30' × 30', adopting the same criteria we used for the spectral analysis, with a resolution of 32 × 32 pixels. The pixel size was chosen to reasonably match the dimension of the elements in Cen's cube. One single element of the box is 195 h⁻¹ kpc by side, equivalent to an angle of about 1 arcmin at a distance of 600 h⁻¹ Mpc (redshift $z \sim 0.18$). The basic idea is to create a three dimensional array. The first two axes represent the angular coordinates of the map, in arcminutes, and the third axis is the energy. Instead of a map we have a “pile” of maps, each representing the photon counts at increasing energy, from 0.05 to 2 keV. From this array is then easy to generate intensity or photon counts maps for different energy intervals.

The procedure to generate the maps was essentially identical to the one discussed

before, with each pixel of the image corresponding to a separate FOV. Also in this case we saved one three-dimensional image for each of Cen’s cubes in the field of view. This gives us pictures of the simulated universe in slices taken at increasing redshift. The simulated images can be used to extract information about the expected angular distribution of the WHIM and to understand the difficulties in extracting information about the WHIM properties from the analysis of real data. To quantify the angular distribution of the X-ray from the WHIM we generated images in the energy interval 0.375 - 0.950 keV and then we used an adaptation of the algorithm described by Soltan (Soltan et al. 1996) and updated by Kuntz (Kuntz et al. 2001) to calculate the Angular Autocorrelation Function (AcF) of the X-ray flux. The amount of clustering on different angular scales is quantified by the AcF:

$$w(\theta) = \frac{\langle I(n)I(n') \rangle}{\langle I^2 \rangle},$$

where $I(n)$ is the intensity of the X-ray background (XRB) in the direction n , $I(n)I(n')$ is the product of intensities with angular separation θ , and $\langle \dots \rangle$ denotes the expectation values of the corresponding quantities. In X-ray astronomy, the radiation distribution is typically represented by an array of photon rates per pixel. As an estimator of the ACF, the expectation values are therefore replaced by the corresponding average quantities. A practical recipe to calculate the ACF, using a weighting of the intensity based on exposure time, is given by Kuntz (2001):

$$w(\theta) = \frac{\sum_{i,i'} (R - \bar{R})(R' - \bar{R}')\sqrt{ss'}}{\sum_{i,i'} \sqrt{ss'}} \cdot \frac{1}{\left[(\bar{R} + \bar{R}')/2 \right]^2},$$

where the sum is over all pairs of pixels separated by θ , R is the photon rate in those pixels, s is the exposure time for those pixels, used as statistical weight, and $\overline{(\dots)}$ denotes the average value. Notice that if a single image is used for the calculations, and N_θ is the

number of pixels separated by θ , then $\overline{R} = \overline{R'}$, and we can write:

$$w(\theta) = \frac{\sum_{i=1, N_\theta} \sum_{j=i+1, N_\theta} (R_i - \overline{R})(R_j - \overline{R}) \sqrt{s_i s_j}}{\sum_{i=1, N_\theta} \sum_{j=i+1, N_\theta} \sqrt{s_i s_j}} \cdot \frac{1}{\overline{R}^2}.$$

In Fig. 5 we show the autocorrelation function calculated for a sample of 40 images. The curves show a similar overall behavior, with some amount of dispersion that was expected from previous investigations (Kuntz et al. 2001). Due to the extension of our images, the value of the AcF is reliable only between 1 arcmin up to about 20 arcmin, after which it degenerates due to the limited sampling of the images. Such interval seems to be more than appropriate to characterize the WHIM behavior. In fact, as the average of all the AcF shows (Fig. 6), there seem to be a clear angular correlation below a few arcminutes, while above 10 arcmin the curve is compatible with zero, indicating a typical angular scale of the WHIM filaments of a few arcminutes. This result and our previous considerations about the presence of a single filament in the FOV indicate that any mission designed to investigate the WHIM should have an angular resolution not worse than a few arcminutes.

5. Conclusions

Based on the output of hydrodynamical simulations, we investigated the properties of the expected X-ray flux from the WHIM. This is of particular relevance in designing a mission optimized to detect and study the properties of the WHIM. Our simulations indicate that such a mission is possible and should be capable of detecting and characterize the WHIM. Moreover, in addition to good energy resolution (necessary to identify redshifted emission lines) and low background (due to the very low photon rate of the WHIM), our analysis shows that such a mission should have an angular resolution of at least a few arcminutes.

We would like to thank Renyue Cen for giving public access to the output of his hydrodynamic simulation. We would also like to thank Mauro Roncarelli and Wilton T. Sanders for the useful discussion and suggestions.

REFERENCES

- Anders, E. & Grevesse, N. 1989, *Geochimica et Cosmochimica Acta*, 53, 197)
- Barber, C. R., Roberts, T. P., Warwick, R. S. 1996, *MNRAS*, 282, 157
- Bennett, C. L. et al 2003, *ApJS*, 148, 1
- Bregman, J. N. & Irwin, J. A. 2001, AAS Meeting, 198, 58.02
- Borgani, S. et al. 2004, *MNRAS*, 348, 1078
- Burles, S., & Tytler, D. 1998, *ApJ*, 499, 699
- Cen, R., Ostriker, J. P. 1999, *ApJ*, 514, 1
- Cen, R., Ostriker, J. P. 2001, *ApJ*, 519, L109
- Croft, R. A. C., et al. 2001, *ApJ*, 557, 67
- Fang, T., et al. 2002, *ApJ*, 572, L127
- Fukugita, M., Hogan, C. J., & Peebles, P. J. E. 1998, *ApJ*, 503, 518
- Galeazzi, M., et al. 2000, *NIM A*, 444, 268
- Galeazzi, M., Ursino, E., Sanders, W. T. 2004, HEAD Eighth Divisional Meeting, 2004, New Orleans, Louisiana, USA, # 03.06, <http://www.aas.org/publications/baas/v36n3/head2004/262.htm>
- Kirkman, D., et al. 2003, *ApJS*, 149, 1
- Kuntz, K. D. et al. 2001, *ApJ*, 548, L119
- McCammon, D., et al. 2002, *ApJ*, 576, 188

- Morrison, R., McCammon, D. 1983, ApJ, 270, 119
- Mulchaey, J. S., et al., 2003 ApJS, 145, 39
- Nicastro, F., et al. 2002, ApJ, 573, 157
- Nicastro, F., et al. 2005, Nature, 433, 495
- Rasmussen, A., 2002, in "High Resolution X-ray Spectroscopy with XMM-Newton and Chandra", Ed. G. Branduardi-Raymont, E34
- Rasmussen, A., et al. 2003, HEAD Seventh Divisional Meeting, 2003, Mt. Tremblant, Quebec, Canada, #02.01,
<http://www.aas.org/publications/baas/v35n2/head2003/251.htm>
- Rauch, M., et al. 1998, ApJ, 489, 1
- Scharf, C., et al. 2000, ApJ, 528, L73
- Soltan, A. M., et al. 1996, A&A, 305, 17
- Soltan, A. M., Freyberg, M. J., Trümper, J. 2001, A&A, 378, 735
- Tripp, T. M. & Savage, B. D. 2000, ApJ, 542, 42
- Weinberg, D. H., Miralda-Escudé, J., Hernquist, L., & Katz, N. 1997, ApJ, 490, 564
- Yoshikawa, K., et al. 2003, PASJ, 55, 879
- Zappacosta, L., et al., 2002, A&A, 394, 7

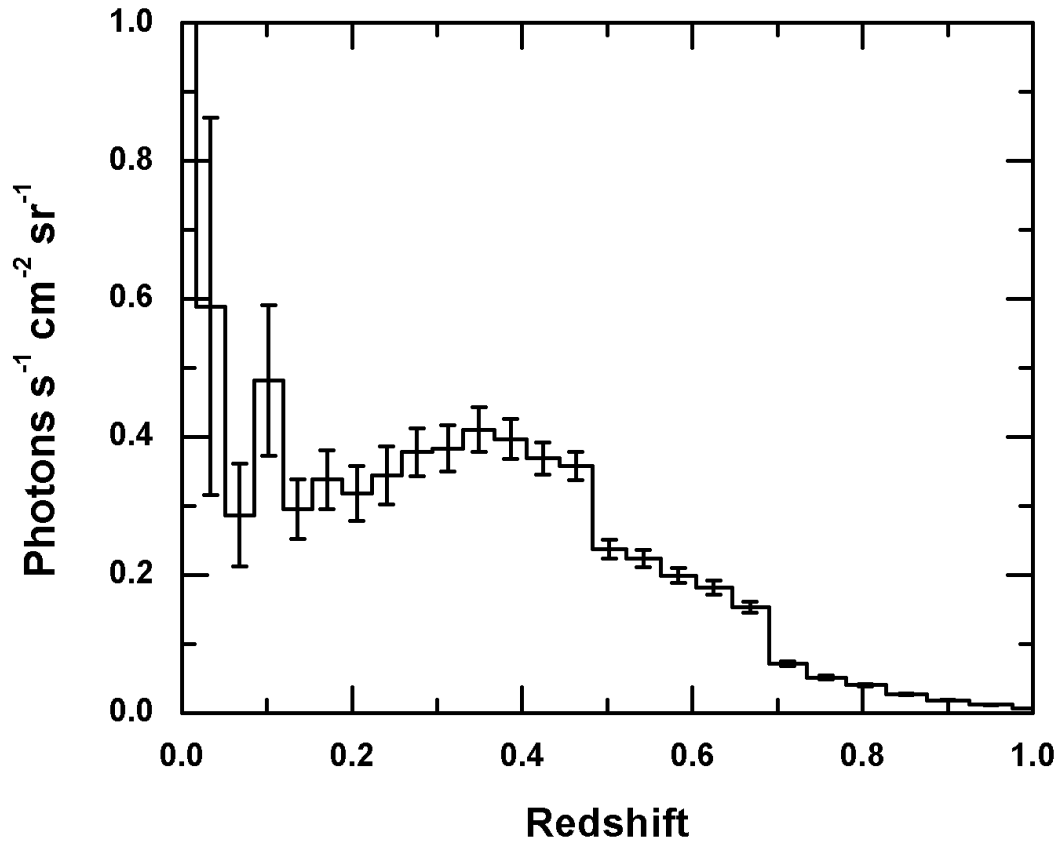


Fig. 1.— Photon flux of the WHIM as a function of the distance from the emitter (redshift).

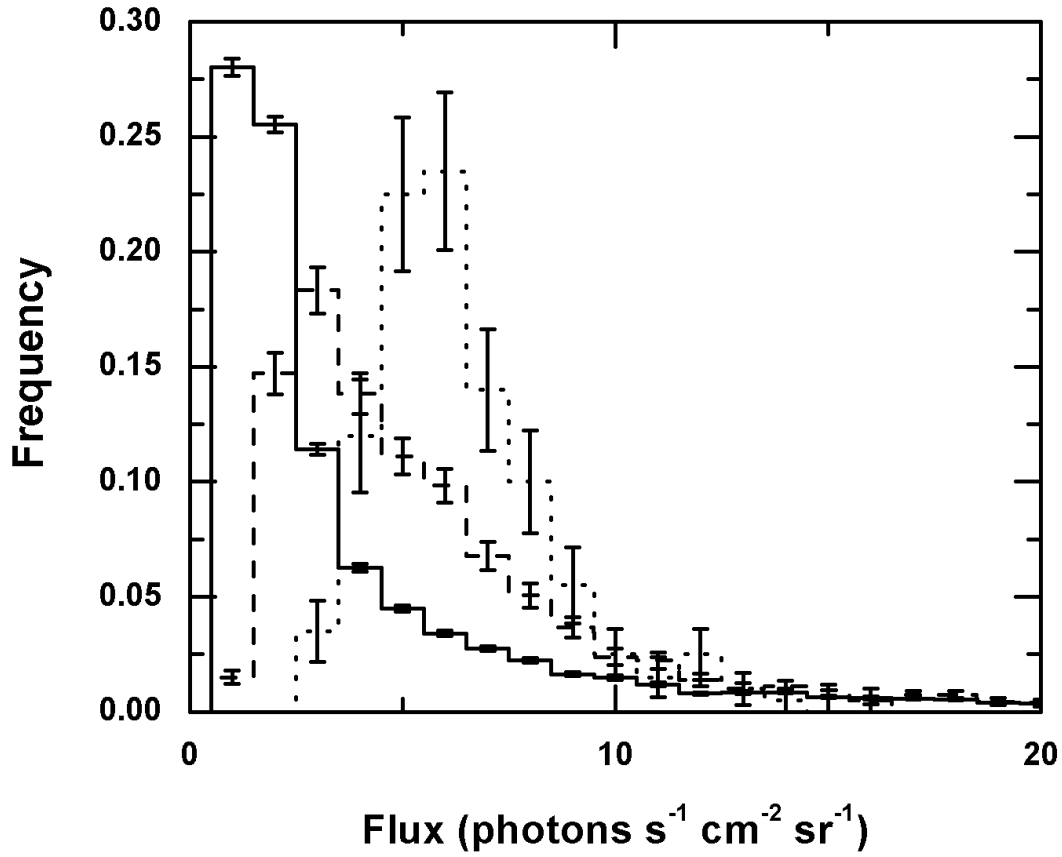


Fig. 2.— Distribution of photon flux of the WHIM for simulations with FOV's of 3' (solid line), 10' (dashed line), and 30' (dotted line).

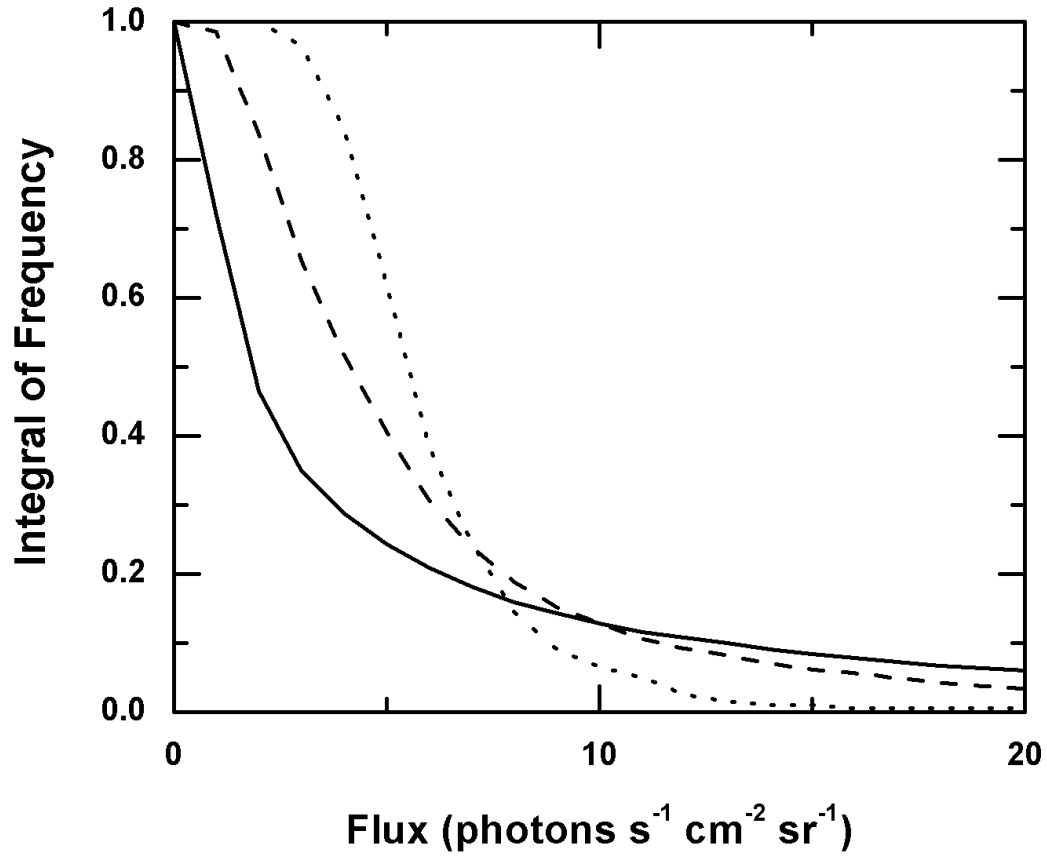


Fig. 3.— Integral of the distribution of photon flux from Fig. 2 for simulations with FOV's of 3' (solid line), 10' (dashed line), and 30' (dotted line).

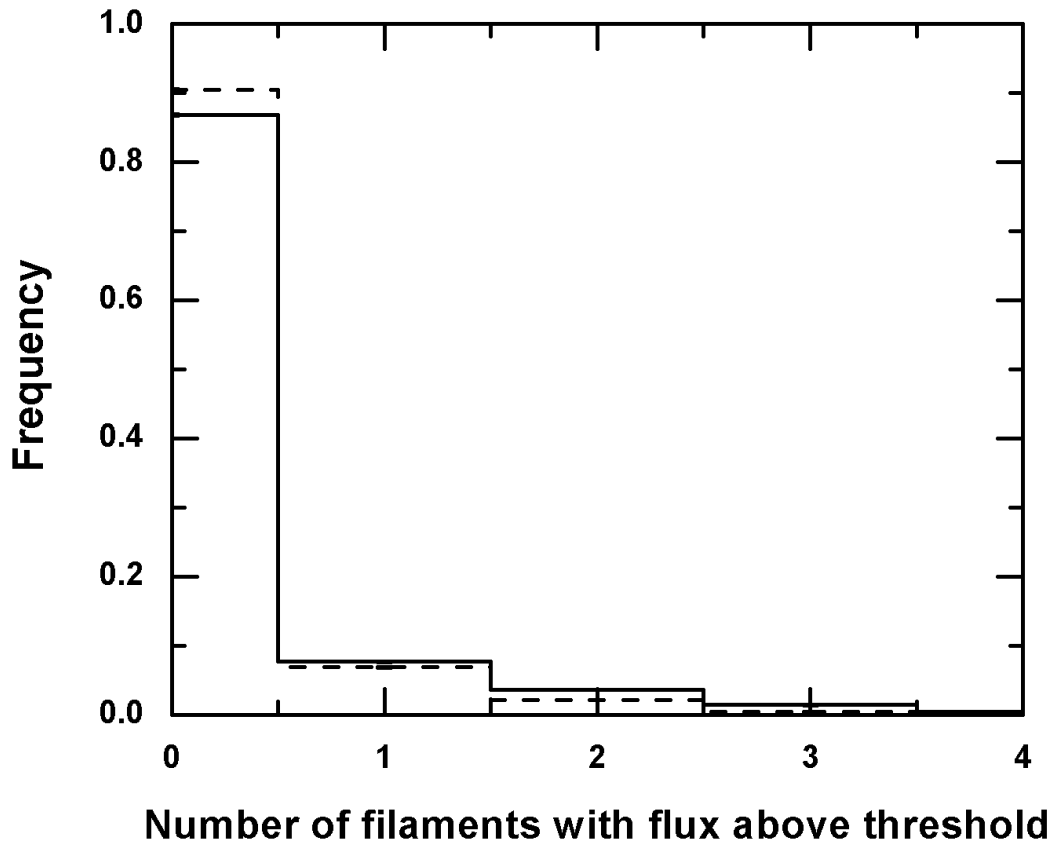


Fig. 4.— Probability of observing, in one simulation, redshift intervals (filaments) with photon flux higher than 10% (solid line) or 20% (dashed line) of the Diffuse X-Ray Background Flux. The data are for simulations with a FOV of 3'.

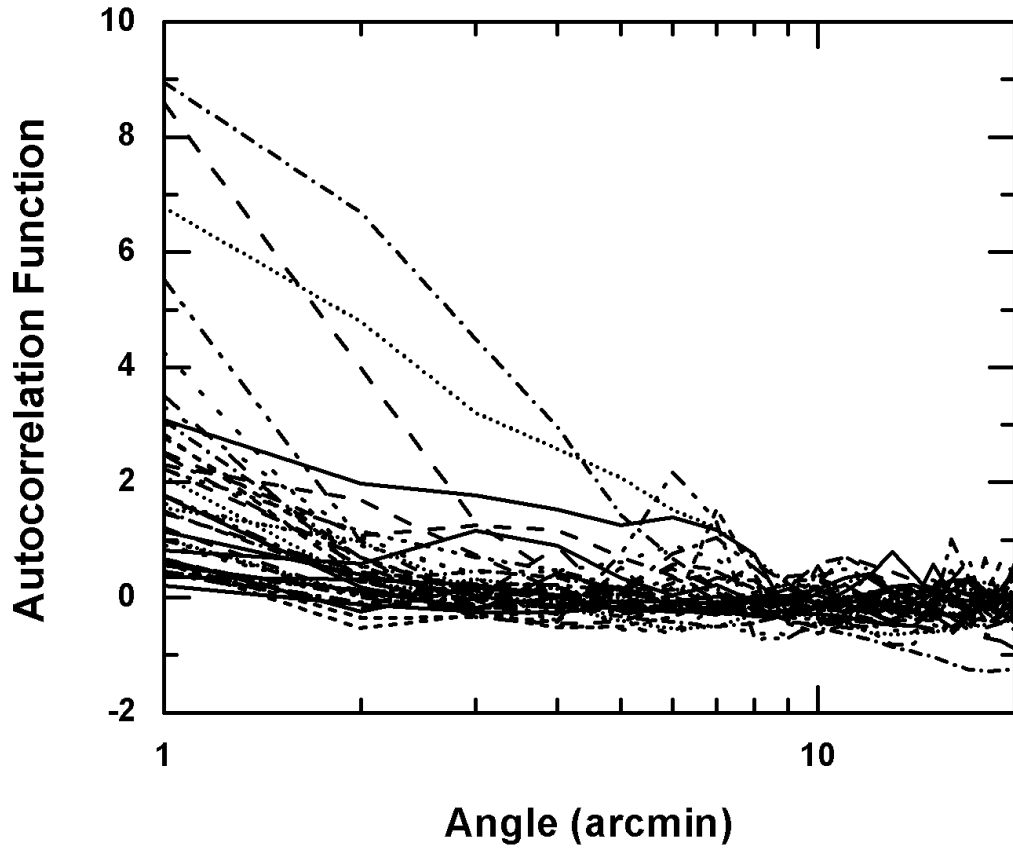


Fig. 5.— Angular Autocorrelation functions of the X-ray in the energy interval 0.375 - 0.950 keV calculated for a sample of 40 images.

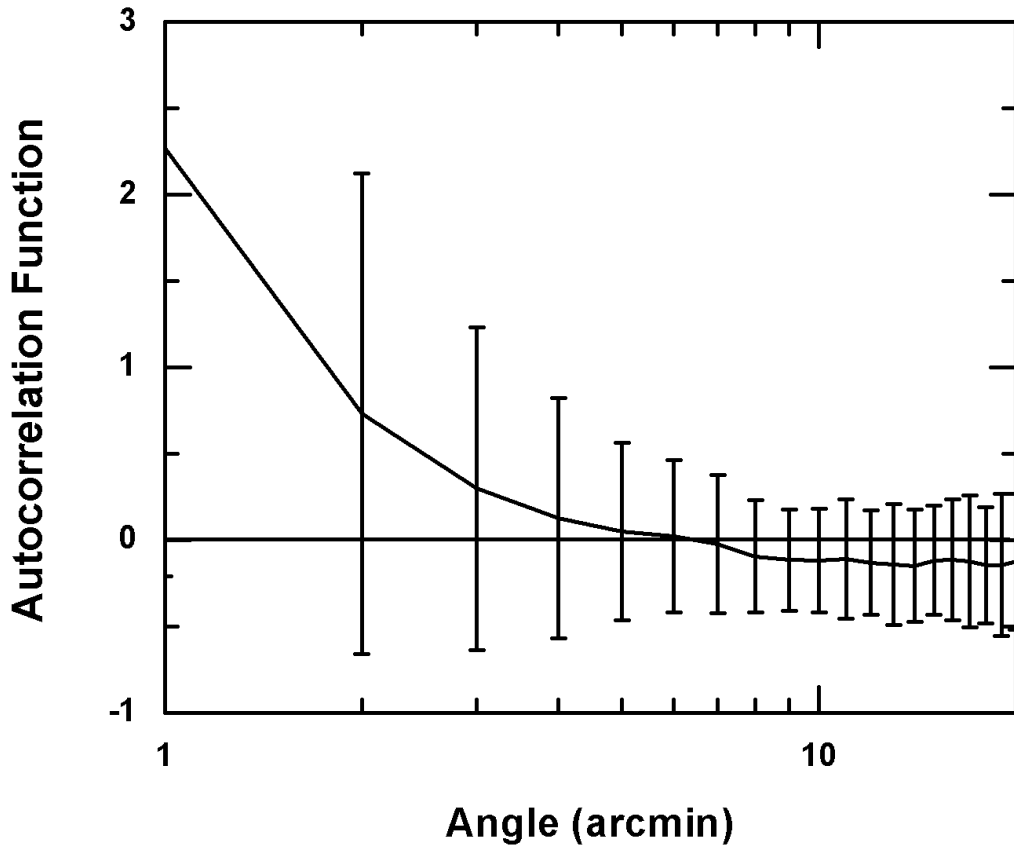


Fig. 6.— Average angular autocorrelation function of the X-ray flux from the WHIM in the energy interval 0.375 - 0.950 keV.